Multiple, coeval silicic magma storage domains beneath the Laguna Del Maule volcanic field inferred from gravity investigations

Sarah F. Trevino[1]; Craig A. Miller[2]; Basil Tikoff[1]; Dominique Fournier[3]; Brad S Singer[1]

[1] Department of Geoscience, University of Wisconsin–Madison, Madison WI, 53706, USA

[2] GNS Science, Wairakei Research Centre, Taupo 3352, New Zealand

[3] Mira Geoscience,512B 409 Granville St. Vancouver, BC V6C 1T2, Canada

Corresponding author: Craig Miller (c.miller@gns.cri.nz)

Key Points: (140 characters max)

- At least two separate magma storage regions in different physical states exist beneath the Laguna del Maule volcanic field
- A -6 mGal gravity anomaly below the Barrancas complex is close to a postulated inflation source which produced ~62 m of Holocene uplift
- Comparing model densities to nearby plutons and seismic models indicates Barrancas magma is above solidus with a small melt proportion.

Abstract

The rhyolite-producing Laguna del Maule volcanic field (LdMVF) records magma-induced surface inflation rates of ~ 25 cm/year since 2007. During the Holocene, ~60 meters of cumulative surface uplift is recorded by paleoshorelines of the Laguna del Maule, located on the southeast edge of the LdMVF (Chile-Argentina border) near the Barrancas volcanic complex. Rhyolites from the Barrancas complex erupted over ~14 ka including some of the youngest (1.4 ± 0.6 ka) lava flows in the field. New gravity data collected on the Barrancas complex reveals a Bouguer low (-6 mGal, Barrancas anomaly) that is distinct from the pronounced gravity low (-19 mGal; Lake anomaly) associated with present-day deformation and magma intrusion to the north. Three-dimensional inversion of the Barrancas anomaly indicates the presence of a magma body with a maximum density contrast of -250 kg/m^3 centered at a depth of ~ 3 km below surface. Comparison of model densities with measured densities from nearby silicic plutons suggest that a magma body, containing < 30 % melt phase and a low volatile content, exists beneath the Barrancas complex. The Barrancas and Lake gravity lows represent magma in different physical states, associated with past and present-day storage beneath the LdMVF. The gravity model mirrors existing geochemical observations which independently indicate that at least two distinct rhyolites were generated and stored as discrete magma bodies within the broader LdMVF. Small temperature changes of these discrete bodies could reverse crystallization and viscous lock-up and propel magma toward a crystal-poor eruptible state.

Plain Language Summary

The Laguna del Maule volcanic field in Chile, has a long history of eruptions that produce large explosions and voluminous lava flows. Lava emitted during these eruptions comes from shallow sources of partially molten rock (magma) located a few kilometers below the surface. Magma intruded from below and into these shallow regions has caused extensive ground deformation around the lake over the last 10,000 years. To understand the causes of deformation and assess the likelihood of future eruptions, it is essential to know the location and present-day state of magma within the crust. Magma is typically less dense than the surrounding rock and these density variations cause small changes in the local gravity field, detectable with geophysical instruments. We collected a new set of gravity measurements at the Barrancas volcanic complex to determine if magma is present beneath the volcano that last erupted about two thousand years ago. Our data reveal a shallow magma body at depth beneath the Barrancas complex. This new magma body is separate from another magma body located in a different part of the Laguna del Maule volcanic field, which has important implications for the assessment of future volcanic hazards in the region.

1 Introduction

Snapshots of the geologic record showing the evolution of shallow silicic plutonic and magmatic systems through to their ultimate expression as explosive and effusive rhyolite eruptions are rare. Recent geochemical and geochronological studies (Glazner et al., 2004; Cooper & Kent, 2014; Barboni et al., 2016; Rubin et al., 2017; Andersen et al., 2017a; 2018; Schaen et al., 2017) of eruptive products and exhumed plutons propose that shallow silicic reservoirs exist as “mush” systems containing discrete batches of eruptible interstitial melt within a larger mostly crystalline framework (Bachmann & Bergantz, 2004; Hildreth, 2004). Over

time, these bodies may cool to form plutons or, with the addition of heat and volatiles delivered via basaltic to andesitic intrusions, melting or defrosting of the mush can rapidly produce eruptible pools of crystal-poor rhyolitic melt (Druitt et al., 2012; Cooper & Kent, 2014; Till et al., 2015; Andersen et al., 2018). These data and models propose a continuum between the end members of cold plutonic storage systems and systems that are heated and incubated such that they may produce explosive eruptions.

Geophysical imaging can provide insight into the location, geometry, and present state of silicic plutonic and magmatic systems (e.g., Magee et al., 2018). Seismic, magnetotelluric, and gravity surveys (Bachmann & Bergantz, 2008; Bertrand et al., 2012; Represas et al., 2012; del Potro et al., 2013; Comeau et al., 2015; Pritchard & Gregg, 2016; Gaynor et al., 2019; Paulatto et al., 2019) have imaged silicic plutonic and magmatic systems in a variety of tectonic settings, including at the LdMVF (Miller et al., 2017a; 2017b; Cordell et al., 2018; Wespestad et al., 2019; Bai et al., 2020; Peterson et al., 2020). These studies inferred the present physical states of magma bodies from the distribution of material properties such as density, conductivity, P and S-wave velocities. However, crustal-scale geophysical models are inherently low resolution that homogenize and smear out anomalous rock volumes, making the petrologic hypothesis of individual melt lenses within the broader crystal matrix difficult to resolve.

The LdMVF comprises at least 40 km^3 of post-glacial (younger than 20 ka) rhyolite encircling a 20 x 16 km lake basin and is thus the largest such concentration of rhyolite erupted in the Andes (Hildreth et al., 2010). Relative to the goals of this study, the LdMVF is an exceptional natural laboratory owing to: (1) rapid rates of surface inflation of over 25 cm/year since 2007 (Feigl et al., 2014; Le Mével et al., 2015; 2016) that have re-accelerated recently (Le Mével et al., 2019), and more than 60 meters of surface warping during the Holocene (Singer et

al., 2018), that reflect active growth of a large underlying magma reservoir system (Singer et al., 2014), (2) The geochronology, petrology, and geochemistry of the LdMVF eruptive products are well documented with mineral compositions revealing at least two physically discrete, chemically distinct, long-lived rhyolite-producing domains in the upper crust (Andersen et al., 2017b; 2018; 2019), and melt inclusions indicating an H_2O-rich, CO_2-charged, magma reservoir system producing rhyolitic liquids from 14 to 4 km depth (Klug et al., 2020), and (3) The late Miocene Risco Bayo-Huemul plutonic complex, exposed only 20 km to the west, spans a compositional range of gabbro to high-silica granite very similar to the LdMVF and is of comparable dimensions to the LdMVF (Schaen et al., 2017; 2018; Garibaldi et al., 2019).

Here we expand the 3D density model of Miller et al. (2017b) to include new gravity data from the Barrancas complex (Sruoga et al., 2015; 2018) in the southern part of the Laguna del Maule volcanic field (LdMVF). Our observations reveal a previously unmapped -6 mGal Bouguer gravity anomaly below the Barrancas complex ("Barrancas anomaly") that is physically independent of the larger (-19 mGal) negative anomaly associated with current surface inflation at LdMVF ("Lake anomaly") (Le Mével et al., 2016; Miller et al., 2017b). We also report new density measurements from granites comprising the nearby Risco Bayo and Huemul plutons (Schaen et al., 2017) as a novel means of exploring the full density evolution of silicic magmas in this part of the Andes. Moreover, we interpret these new geophysical data in context of the extensive petrological (Andersen et al., 2017b, 2018, 2019; Cáceres et al., 2018; Klug et al., 2020) and geomorphic (Singer et al., 2018) findings from LdMVF. This multidisciplinary approach allows us to reduce the non-uniqueness inherent in geophysical models and to better understand the hazards posed by silicic magma systems (Till et al., 2018). Our high-resolution

109 geophysical observations of the broad magmatic system at LdMVF images multiple embedded
110 magma bodies, in different developmental stages within a large silicic reservoir.

111 ## 2 Geologic setting and previous work

112 The Laguna del Maule volcanic field (LdMVF) (Fig. 1), located on the crest of the Andes
113 (36° S) within the Southern Volcanic Zone, comprises the region's largest concentration of
114 crystal poor rhyolite and has hosted at least 50 post-glacial rhyolitic eruptions comprising >40
115 km^3 since 25 ka (Andersen et al., 2017b; Hildreth et al., 2010). The LdMVF lies 20-30 km south
116 east of the 7.2 to 6.2 Ma Risco Bayo and Huemul plutonic complexes (Schaen et al., 2017, 2018;
117 Garibaldi et al., 2018). The Huemul pluton is a high silica granite that is inferred to reflect
118 residual melt extracted from crystal cumulates (Schaen et al., 2017). These plutons are
119 interpreted as frozen magma reservoirs that solidified at 4-6 km depth analogous to those that
120 likely are growing beneath the present day LdMVF (Schaen et al. 2017; Le Mevel et al., 2016;
121 Andersen et al., 2017b; 2018; Wespestad et al., 2019). As such, they offer a unique perspective
122 on how the LdMVF magmatic system has evolved that is complimentary to that derived solely
123 from the eruptive products of the LdMVF.

124 Plagioclase and zircon petrochronologic data reveal that the two distinct eruptive
125 episodes at 23-19 ka and 8–2 ka also reflect rhyolite generation in compositionally and
126 physically distinct domains beneath the LdMVF (Andersen et al., 2018; 2019). The four
127 youngest vents and eruptive complexes are in the south and eastern part of the LdMVF,
128 suggesting that this region once contained a significant volume of eruptible melt. The youngest
129 eruptions, dated by $^{40}Ar/^{39}Ar$ methods or inferred from geomorphology, are the Cari Launa (<3.3
130 ±0.6 ka), the rhyolite of Colada Divisoria (2.1 ± 0.7 ka), Colada Las Nieblas (~1.8 ka), and the
131 Barrancas complex (14.5-1.9 ka) (Andersen et al., 2017b, 2019). The Colada Las Nieblas flow

lacks pumice cover and displays an uneroded morphology and is considered of comparable age to the younger portions of the Barrancas complex and eastern Barrancas complex lavas (around 2.1 to 1.9 ka). The $^{40}Ar/^{39}Ar$ chronology is supported by ^{36}Cl surface exposure dates of 2.5 ± 0.7 ka and 1.4 ± 0.6 ka for the youngest Barrancas flows (Singer et al., 2018). In addition, the younger flow from the Cari Launa vent yields an imprecise ^{36}Cl surface exposure date of 0.8 ± 0.6 ka, indicating a late Holocene age (Singer et al., 2018).

Within the LdMVF, the Barrancas volcanic complex is distinctive because it is the site of multiple dome forming episodes within the last 14 ka and contains some of the youngest (1.4 ± 0.6 ka) erupted lavas of the LdMVF. Between 14.5 and 8.4 ka at the LdMVF, rhyolite erupted only from the Barrancas complex and eruptive material from Barrancas forms a large portion (~ 6 km^3) of the post Last Glacial Maximum eruptive history of LdMVF. The western Barrancas dome complex was constructed between 14.5 and 11.4 ka and partially collapsed to produce large block and ash flows that traveled ~13 km filling valleys with deposits ~60 - 120 m thick, decreasing to 10 m in distal areas (Fig. 1; Sruoga et al., 2015, 2018). The younger eastern domes (5.6 to 1.4 ka) produced 8 obsidian flows and several tephra falls and pyroclastic flows. The Barrancas domes show the only evidence of shallow hydrothermal alteration in the LdMVF. Advanced argillic alteration has affected these domes, as well as block and ash flow deposits, suggesting that circulation of > 300 °C hydrothermal fluids may have contributed to dome collapse (Sruoga et al., 2018).

The Barrancas rhyolites are distinguished from the older 22-19 ka rhyolites erupted in the north from a magma source coincident with the Lake gravity anomaly by their elevated Sm and Y abundances, low TiO_2 in magnetite, and high Ce in plagioclase crystals (Andersen et al., 2017b; 2018; 2019; Klug et al., 2020). The Barrancas rhyolites show no evidence for having

155 mixed with other spatially discrete rhyolites, strongly suggesting compartmentalization of
156 eruptible domains within the wider magma reservoir (Andersen et al., 2018; 2019).

157 Petrologic evidence from melt inclusion composition and entrapment pressures (Klug et
158 al., 2020) suggests that crystal poor rhyolite melt beneath the LdMVF accumulated in the
159 shallow crust (50 – 350 MPa, ~ 2 to 8 km depth) after ascending out of rhyodacitic mush at ~8 –
160 14 km. The crystal poor rhyolite accumulation pressures derived from melt inclusions are at the
161 lower end of those derived from analysis of amphibole crystals in the rhyodacites (Andersen et
162 al., 2017b; Cáceres et al., 2018) that suggest crystallization pressures of 190 – 400 MPa. The
163 voluminous rcb-py pyroclastic flow on the south flank of the Barrancas complex (Fig. 1) has
164 some of the lowest melt inclusion derived pressures (50 – 150 MPa) from LdMVF, consistent
165 with its origin via collapse of shallowly emplaced, and thoroughly degassed, endogenous and
166 exogenous domes (Sruoga, et al., 2018; Klug et al., 2020).

167 The summit of the Barrancas complex is < 5 km south of a high stand paleoshoreline that
168 formed when the lake was dammed by the Espejos rhyolite coulée at 19.0 ka and is inferred to
169 have been a horizontal surface when the lake catastrophically drained at 9.4 ka. The present day
170 paleoshore is uplifted 62 m in the southern part of the lake basin relative to the northern part.
171 This pattern is consistent with surface warping produced by an inflating magma reservoir located
172 below the southeastern portion of the lake basin, beneath the northern flank of the Barrancas
173 complex (Singer et al., 2018).

174 The identification of rapid surface inflation within the LdMVF, at rates greater than 25 cm/yr
175 since 2007, has prompted several geophysical studies that have imaged a trans-crustal magma
176 system and a small upper crustal fault system beneath the eponymous lake using teleseismic
177 tomography (Bai et al., 2020), surface wave tomography (Wespestad et al., 2019), seismic

178 reflection and magnetics (Peterson et al., 2020), magnetotellurics (Cordell et al., 2018, 2019,
179 2020), geodesy (Feigl et al., 2014; Le Mével et al., 2015, 2016; Zhan et al., 2019), and gravity
180 (Miller et al., 2017b). Gravity inversion, teleseismic tomography, and surface wave tomography
181 show overlapping low-density and low-velocity anomalies (referred to here as the "Lake"
182 anomaly) interpreted as a crystal-rich, dacitic to rhyodacitic magma reservoir occupying between
183 100 and 500 km^3 at depths between 2 and 12 km, containing domains including 20-70 km^3 of
184 volatile-rich rhyolite melt that is spatially coincident with the deformation source. Teleseismic
185 and surface wave tomography suggests that melt contents in the Lake magma body range from 5
186 – 14 %, however these are likely to be minima due to inherent vertical smearing and wide grid
187 cell widths (3 to 4 km) (Wespestad et al., 2019; Bai et al., 2020).

188 Teleseismic tomography (Bai et al., 2020) also resolves a low-Vp anomaly in the southeast of
189 the LdMVF beneath the Barrancas complex. This feature is elongated northeast-southwest, dips
190 to the southwest, and is resolvable to about 25 km depth. The velocity perturbation of this
191 feature is -100 to -200 m/s compared to -400 m/s for the main Lake anomaly. However, its
192 location on the edge of the seismic array leads to greater uncertainty as to the geometry of this
193 feature. Group velocity maps from surface wave tomography show a negative group velocity
194 anomaly across the 0.29 to 0.39 Hz range in the southeast corner of the basin towards the
195 Barrancas complex suggesting a melt phase may be present (Wespestad et al., 2019).

196 Using 3D MT inversion, Cordell et al. (2018, 2020) imaged the deeper portion of the magma
197 system that extends north of the lake and likely represents a deep crustal zone of magma storage,
198 mixing, and assimilation (Andersen et al., 2017b). The Barrancas complex is on the edge of the
199 MT array, although there is a suggestion of a shallow (~1-3 km) conductive body (~10 Ωm)
200 beneath Barrancas, below which (> 4 km) are more resistive rocks (> 100 Ωm).

Together the geophysical observations strongly point to a trans-crustal magma system extending to within 2 km of the surface, which is consistent with the petrologic and geochemical observations. Imaging of the Lake anomaly and identification and modeling of the source of paleoshoreline warping prompted further geophysical investigation of the Barrancas complex, which was on the edge of previous geophysical imaging campaigns.

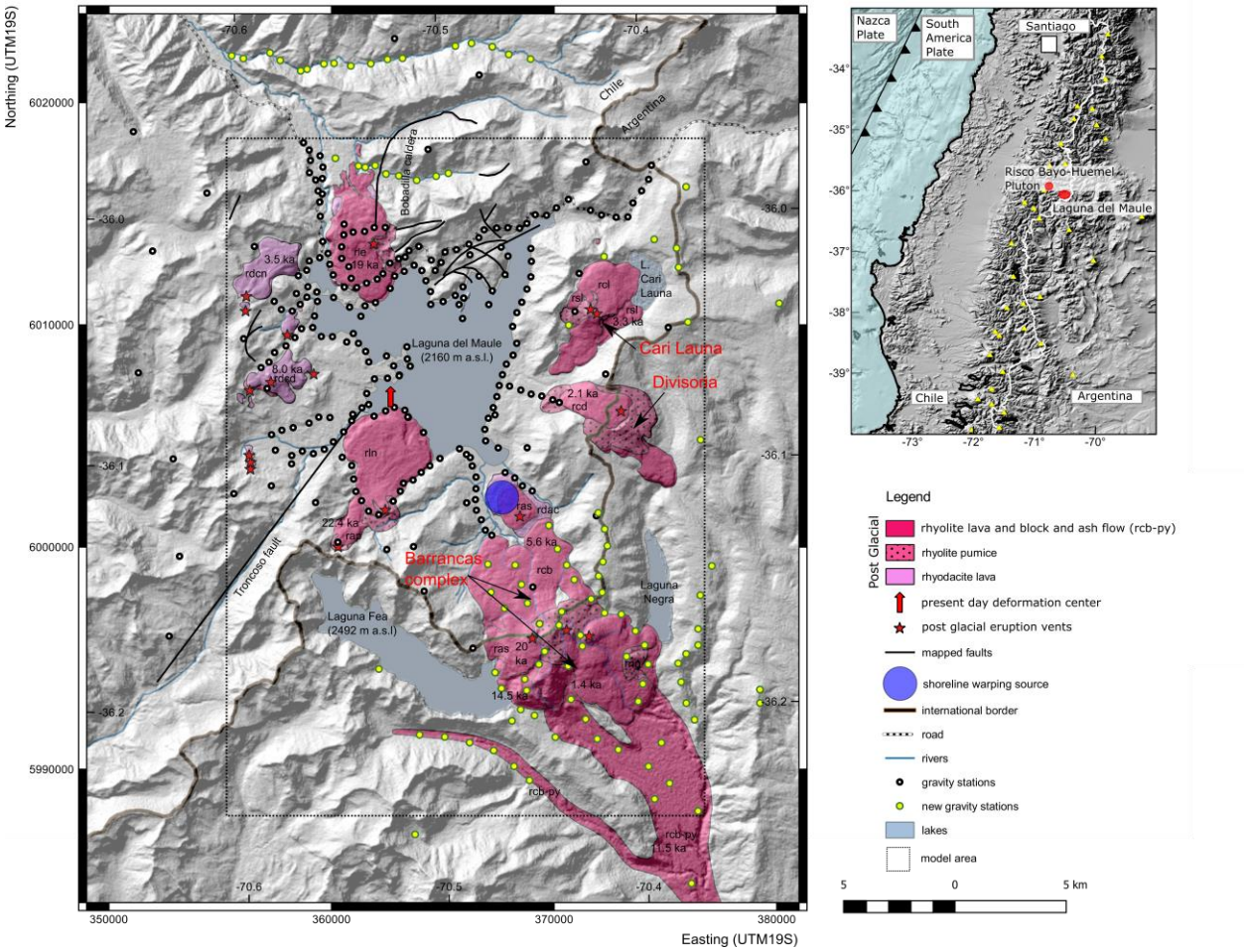

Figure 1. Geological map of the Laguna del Maule volcanic field showing post glacial silicic lavas and pyroclastic deposits. White dots are the gravity data from Miller et al. (2017b), yellow dots are new data from this study. Modified from Miller et al. (2017b) and Andersen et al. (2017b).

3 Data

3.1 Gravity data

We collected 105 additional terrestrial gravity measurements over two summer campaigns in December 2017 and March 2018, building on the work of Miller et al. (2017b) (Fig. 1). Measurements were taken every 500–1000 m in a series of 3–4 km long, radial and valley parallel profiles within a 15 km radius of the main Barrancas complex. Of the 105 measurements, 19 were collected in two E-W transects in valleys north of the lake and four far-field gravity measurements were collected south and east into Argentina to improve the regional gravity field definition. For precise positioning we used a Leica 530 GPS receiver with 15-minute occupation time per station; with maximum baseline lengths of 10 km to the Observatorio Volcanológico de Los Andes del Sur (OVDAS) CGPS network in Chile, we obtain height errors of better than 15 cm (~0.045 mGal) at 95% confidence level.

Daily raw gravity data was corrected for Earth tide and drift using Gtools (Battaglia et al., 2012), to produce gravity values relative to the local base. Local gravity values were converted to absolute values using two nearby absolute gravity stations (Miller et al., 2017b). Gravity data were corrected to the ellipsoid height datum, as our heights are derived from GNSS measurements referenced to the WGS84 ellipsoid and follow the complete Bouguer anomaly data reduction scheme outlined in Hinze et al. (2005). Calculation of the reference density, which represents the average density of the crust above the reduction datum, using topographic correlation methods (Nettleton, 1939; Parasnis, 1966) yields densities of 2375 and 2361 kg/m^3 respectively. A similar analysis of a commercial dataset (Energy Development Corporation) from the nearby Mariposa geothermal prospect yields values of 2350 and 2452 kg/m^3, while conversion of the OVDAS 1-D P-wave velocity model to density using the relationship of (Brocher, 2005), yields densities of 2429 to 2448 in the top 7 km. The average of all the density

237 determinations is 2413 kg/m^3 that we approximate as 2400 kg/m^3 for use in the gravity reduction.
238 Continental scale gravity models (Tašárová, 2007; Folguera et al., 2012) of the south-central
239 Andes, around latitude 36°S obtain an upper crustal density of 2450 kg/m^3, so our local scale
240 density values are similar to larger continental-scale values.

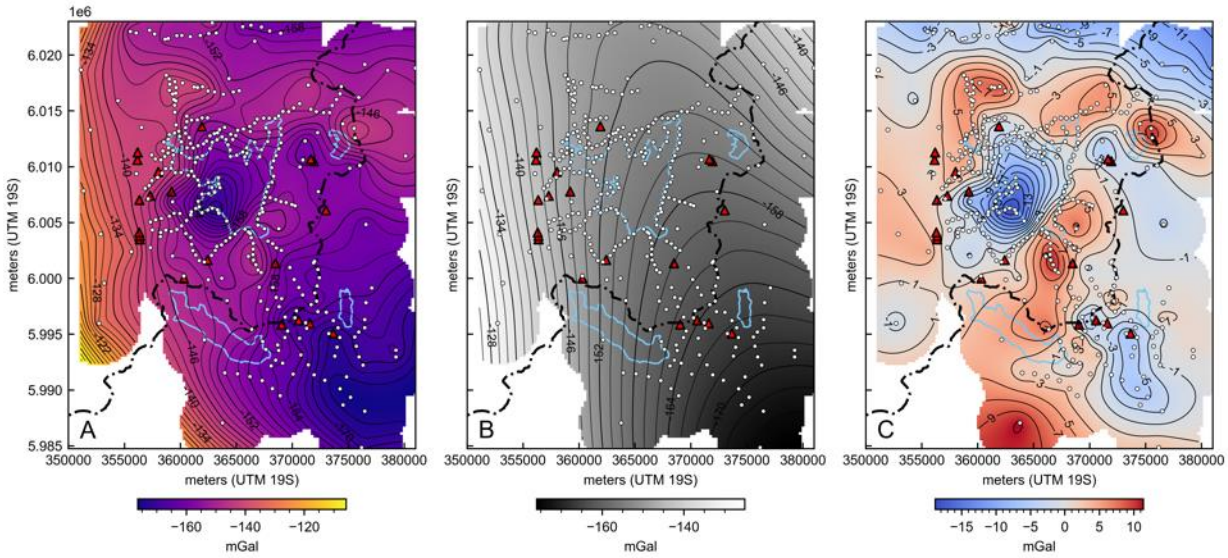

241
242 **Figure 2.** Gravity data collected at the Laguna del Maule volcanic field. A) Bouguer anomaly map, B) Second order
243 regional field, C) residual gravity anomaly. Red triangles are post-glacial eruption vents. The dot-dashed line is the
244 Chile – Argentina border and the lakes are outlined in light blue. Post-glacial eruption vents are red triangles, and
245 white dots are gravity station locations.

246

247 The new dataset was merged with the published (Miller et al., 2017b) gravity data to
248 produce an expanded Bouguer anomaly map of the LdMVF (Fig. 2). The new Bouguer anomaly
249 map identifies a gravity low on the southeast region of the LdMVF, spatially coincident with the
250 Barrancas complex and distinct from the gravity low beneath the lake (Fig. 2A). A second-order
251 polynomial fitted to the data (Uieda, 2018) (Fig. 2B) best approximates the measured regional

field gradient oriented approximately parallel to the South American/Nazca tectonic plate boundary and reflects the eastward dipping subducting plate. We removed the second-order polynomial from the Bouguer anomaly data to produce a residual gravity anomaly dataset suitable for inversion. Experiments with removing first- and third-order polynomials to approximate the regional field produce similar residual anomalies to the 2nd order, which we prefer as it is the lowest order surface that approximates the regional anomaly.

The new residual gravity map (Fig. 2C) shows the previously identified Lake anomaly (Miller et al., 2017b), as well as two more low gravity anomalies in the east of the field spatially associated with the Barrancas complex and Cari Launa vents. A -6 mGal anomaly is located on the southeastern flank of the Barrancas complex. The Barrancas anomaly consists of a small lobe located beneath the summit of the Barrancas eruption vents and the rest of the anomaly extends 5 km to the SE. The southern part of the Barrancas anomaly is broadly coincident with the location of a ~ 60 - 120 m thick valley filling block and ash flow deposit (Sruoga et al., 2015) that was emplaced south of the main volcanic domes and vents at 11.5 ka. It is possible that part of the gravity anomaly reflects this pyroclastic material which we investigate further in the discussion. A -3 mGal anomaly is associated with the Cari Launa and Divisoria vents, however it is not particularly well resolved as station coverage is sparser in this area.

3.2 Density estimates from plutonic rocks

Density measurements of plutonic intrusive rocks that represent an end member state of silica magma systems, are important to aid interpretation of densities derived from gravity models of silicic systems. Plutonic rocks are often inferred to represent the “frozen”, sub-solidus cumulates of magma reservoirs (Glazner et al., 2004; Bachmann et al., 2007). The 7.2-6.2 Ma, high silica granites in the Huemul pluton, located 30 km NW of the LdMVF, are interpreted to

be the frozen remnants of a once eruptible, crystal-poor, rhyolitic melt (Schaen et al., 2017; 2018). This melt is inferred to be extracted out of deeper residual mush at pressures of 100 to 200 MPa or about 3.7 to 7.2 km depth, but not necessarily erupted. This interpretation is consistent with numerical models that consider crustal rheology, exsolved volatile contents, and magma recharge which imply a narrow depth range, 6 to 8 km (200 ± 50 MPa), where silicic magma reservoirs can incubate large bodies of potentially eruptible rhyolite (Huber et al., 2019).

Petrologic and structural studies of the Risco Bayo and Huemul plutons (Schaen et al., 2017; 2018; Garibaldi et al., 2018) have revealed miarolitic cavities and rock fabrics indicative of volatile and melt transport through an underlying crystal mush, including accumulation of vapor bubbles at the roof of the reservoir. These observed features are similar to those proposed to exist within the present-day magma body represented by the Lake anomaly (Miller et al., 2017b; Andersen et al., 2018). As such, the geochemical composition and observed textures of these exhumed granites make them an ideal, crystallized, end-member representative of a present-day silicic melt storage system.

Direct density measurements of the high silica granites can be compared to geophysically derived densities of the nearby silicic melt storage system at LdMVF to provide constraints for interpreting the gravity anomalies. Density measurements were conducted using a glass pycnometer on two to five specimens per intrusive unit of the Risco Bayo – Huemul plutonic complex (Table 1).

Table 1: Density Measurements

Geologic Unit	**No. of Samples**	**Avg. density (kg/m^3)**	**St. dev. (kg/m^3)**	**SiO_2 content (Schaen 2018)**
Huemul high silica	5	2439	15	75-77

granite				
Huemul granite	5	2502	46	68-70
Risco Bayo granodiorite	5	2544	7	62-66
Huemul quartz. monzonite	5	2546	21	62-63
Risco Bayo microdiorite	5	2642	18	55
Risco Bayo gabbro	2	2699	-	51

We measured the densities of a suite of samples spanning the observed compositional range from gabbro to high silica granite at the Risco Bayo and Huemul plutonic complex. The density range varies by 260 kg/m^3 reflecting the density increase from high silica granite to silica poor gabbro. Samples from the Huemul high silica granite - which is interpreted to be the solidified analog of a crystal poor, high silica melt extracted from the granite cumulate framework - have an average density of 2439 kg/m^3 ± 15 kg/m^3. Density measurements of high silica granite samples that contain miarolitic cavities varied by < 10 kg/m^3 from cavity free samples. As we only sampled a fraction of the entire pluton, it is possible there are regions with greater cavity abundance that could more significantly lower the density of the high silica granite. The samples representing the cumulate residual phase have an average density of 2502 kg/m^3 ± 46 kg/m^3. The Bouguer correction density of 2400 kg/m^3 means that if plutonic rocks, such as found are Risco Bayo and Huemul plutons, are present within the survey area, they should create a small positive gravity anomaly.

4 Gravity Inversion Method

To determine the density distribution within the subsurface, we developed a 3D inversion model using a Gauss-Newton, gradient-based approach, implemented in the open source SimPEG framework (Cockett et al., 2015). We implement a mixed L_p norm inversion scheme, with a summary described below.

We construct a 3D mesh with 250 x 250 m horizontal cell size, with vertical cell size increasing by a factor of 1.2 from 100 m in the top 500 m, to 420 m at the base of the grid at -7000 m a.s.l., resulting in 451935 cells. We added 5 layers of padding cells in the horizontal dimensions outside the data coverage to reduce edge effects. The mesh covers a subset of the Bouguer gravity anomaly where the station density is highest, using 306 of the 342 stations (rectangular box in Figure 1). Note that there is no interpolation of data in the inversion routine, only the measured gravity data are used.

As proposed by (Tikhonov & Arsenin, 1977), the inverse problem can be formulated as an optimization problem of the form:

$$\phi(\mathbf{m}) = \phi_d(\mathbf{m}) + \beta\phi_m(\mathbf{m})$$

where β is the tradeoff or Tikhonov parameter. A small β results in a model that fits the data very well but may include excessive structure so that $\phi_m(\mathbf{m})$ is large. Conversely if β is large, the optimization results in a large $\phi_d(\mathbf{m})$. The optimization is nonlinear, so a gradient-based, Gauss-Newton method is used. To run the inversion, we search for a perturbation of the model that reduces the objective function. The iterative optimization process continues until the algorithm converges to a minimum and the misfit tolerance is achieved.

The optimal solution is found at the minimum of the objective function $\phi_m(\mathbf{m})$ which is made up of two terms: 1) The data misfit; and 2) The regularization scheme. Data misfit is a metric which measures the difference between observed and predicted data. The regularization is a metric that is constructed to evaluate the model's agreement with assumptions and prior knowledge. We define the data misfit of the model $\Phi_d(\mathrm{m})$ as:

$$\phi d(m) = \frac{1}{2}\|\boldsymbol{W}_d(F[m] - \boldsymbol{d}_{obs}\|\frac{2}{2}$$

where $\boldsymbol{d}_{obs}$ is the observed data, $F[m]$ is a forward model that produces predicted data, and $\boldsymbol{W}_d$ is a diagonal matrix with elements equal to $\boldsymbol{W}_{d_{ii}} = 1/E$ where E_{ii} is the standard deviation of the *i*th data point. We set E to 0.1 mGal for our model.

The second element is the regularization function. With any inverse technique choice of regularization parameters, it is important to control the final form of the model. Regularizations can be tuned to produce smooth or compact models depending on the prior knowledge of the interpreter. We follow the procedure of Fournier and Oldenburg (2019) such that sparsity assumptions are introduced though a Scaled Iteratively Re-weighted Least Squares (S-IRLS) method. The regularization function reduces to weighted least-squares problem of the form:

$$\phi_m = \sum_{i=u,v,w} \sum_{j=s,x,y,z} \alpha_{i_j} \left\| \mathbf{W}_r \mathbf{R}_{i_j} \mathbf{D}_{i_j} \mathbf{P}_i \kappa_e \right\|_2^2$$

where the projection matrices $\mathbf{P_i}$ select individual component of the vector model. The gradient terms D_x, D_y, D_z are finite difference operators measuring the model roughness along the three Cartesian directions, and D_s is simply the identity matrix. Hyperparameters α j allow the user to change the relative influence of each term.

Sparsity weights R_j are calculated as:

$$R_j diag = \gamma_j \left[\left(\left(D_j \, m^{(k-1)} \right)^2 + \epsilon_j^2 \right)^{p_j/2-1} \right]^{1/2}$$

such that weights depend on the model obtained at a previous k^{th} iteration. The γ_i scaling parameters are used to balance the contribution of different l_p-norm based on the maximum derivatives. This regularization function is flexible and allows us to explore a range of possible solutions by varying the p_i values, where $0 \leq p \leq 2$. Our regularization norm is made up of four

terms, the first term represents the amplitude (density) and the second to fourth terms, the 3 directional gradients.

Instead of deciding on a single regularization we choose to implement many, using all combinations of l_p. We then combine the models into a single median model. In our workflow, we run a twostep inversion process, firstly inverting the data with a `smooth' constraint imposed with a L_2 norm. Secondly, we compute a range of models using a l_p norm, where $0 \leq p \leq 2$. 0 creates compact models while 2 creates smooth models, and 1 is intermediate. For our modeling we keep the 3 gradient terms equal and vary the amplitude term to create 9 possible models with norms [0,0,0,0], [0,1,1,1], [0,2,2,2], [1,0,0,0], [1,1,1,1], [1,2,2,2], [2,0,0,0], [2,1,1,1], [2,2,2,2]. For example, the regularization [0111] places a 0 norm on the density amplitude and 1 norms on the three amplitude gradients. We then calculate the median model from the complete suite of models. This approach also allows us to calculate the probability of a density value occurring in a model cell, importantly providing a method of assessing uncertainty of the model.

Figure 3 illustrates the effect of the different inversion norms on the model. Note that all the models fit the data within the error of the data. From this range of models, we calculate the median model and use the model ensemble to calculate the probability of a density value occurring in each cell.

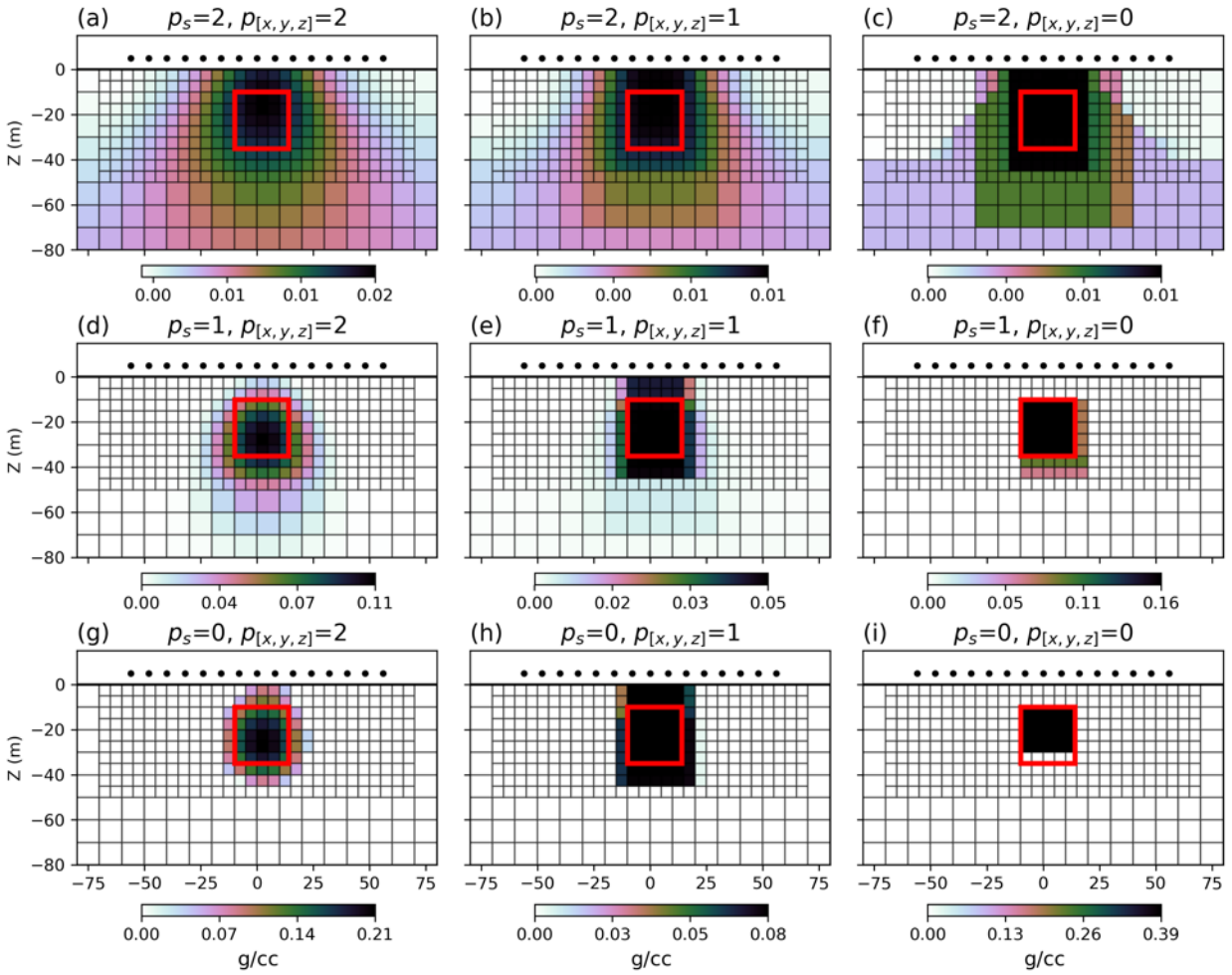

Figure 3. Illustration of different model norms on the final model from a synthetic dataset. The input model outline is shown by the red square and has a density contrast of 0.4 g/cc. The top row (a-c) show norms with a smooth amplitude constraint i.e. [2,2,2,2], [2,1,1,1], [2,0,0,0]. The middle row (d-f) shows models with an intermediate amplitude constraint, i.e. [1,2,2,2], [1,1,1,1], [1,0,0,0] and the bottom row (g-i) shows models with a compact amplitude constraint, i.e. [0,2,2,2], [0,1,1,1], [0,0,0,0].

5 Inversion Model Results and Uncertainty

Depth slices at 1600 and 1100 m a.s.l. (Fig. 4A, B) display a patchwork of high- and low-density regions reflecting near surface variations in lithologies (denser lavas vs. thick pyroclastic material). The most significant of these shallow low-density regions is at the eastern end of Laguna Fea (Fig. 5) and represents an accumulation of pyroclastic material that dams the lake.

384 Below 0 m a.s.l the negative density contrast anomalies coalesce into 3 regions: 1) The
385 Lake anomaly; 2) The Barrancas anomaly and; 3) The Cari Launa and Divisora anomalies,
386 although the model is poorly constrained in later area by sparser data coverage. Figure 5 shows
387 the three-dimensional representation of these bodies as isosurfaces of <1900 kg/m^3 (red) and
388 2200 to 2300 kg/m^3 (grey).

389 The Lake anomaly - identified by Miller et al. (2017b) and Wespestad et al. (2019) - is
390 interpreted to a represent a magma reservoir containing a 20-30 km^3 interstitial melt volume
391 localized within a larger (>100 km^3) crystal rich mush. In this paper we focus on the
392 interpretation of the newly identified Barrancas and Cari Launa anomalies.

393 Our model reveals a 64 km^3 low-density body beneath the rng vent (Fig. 1) on the south-
394 east part of the Barrancas complex that extends from near surface to 4 km below sea level
395 beneath which model resolution becomes poor (Fig.4 X-X' and Z-Z' sections). This body has a
396 maximum density contrast of around -220 kg/m^3 or an estimated absolute density of 2180 kg/m^3.

397 North of the Barrancas complex, our model reveals a shallower anomaly in the
398 subsurface beneath the Cari Launa and Divisoria vents that extends to around 2 km below sea
399 level (Fig 4; W-W' and Z-Z' sections). This 51 km^3 low-density body is resolved with a density
400 contrast of -100 to -150 kg/m^3 or 2250 to 2300 kg/m^3 absolute density. These anomalies are
401 poorly constrained by the data due to a lack of measurements from that region.

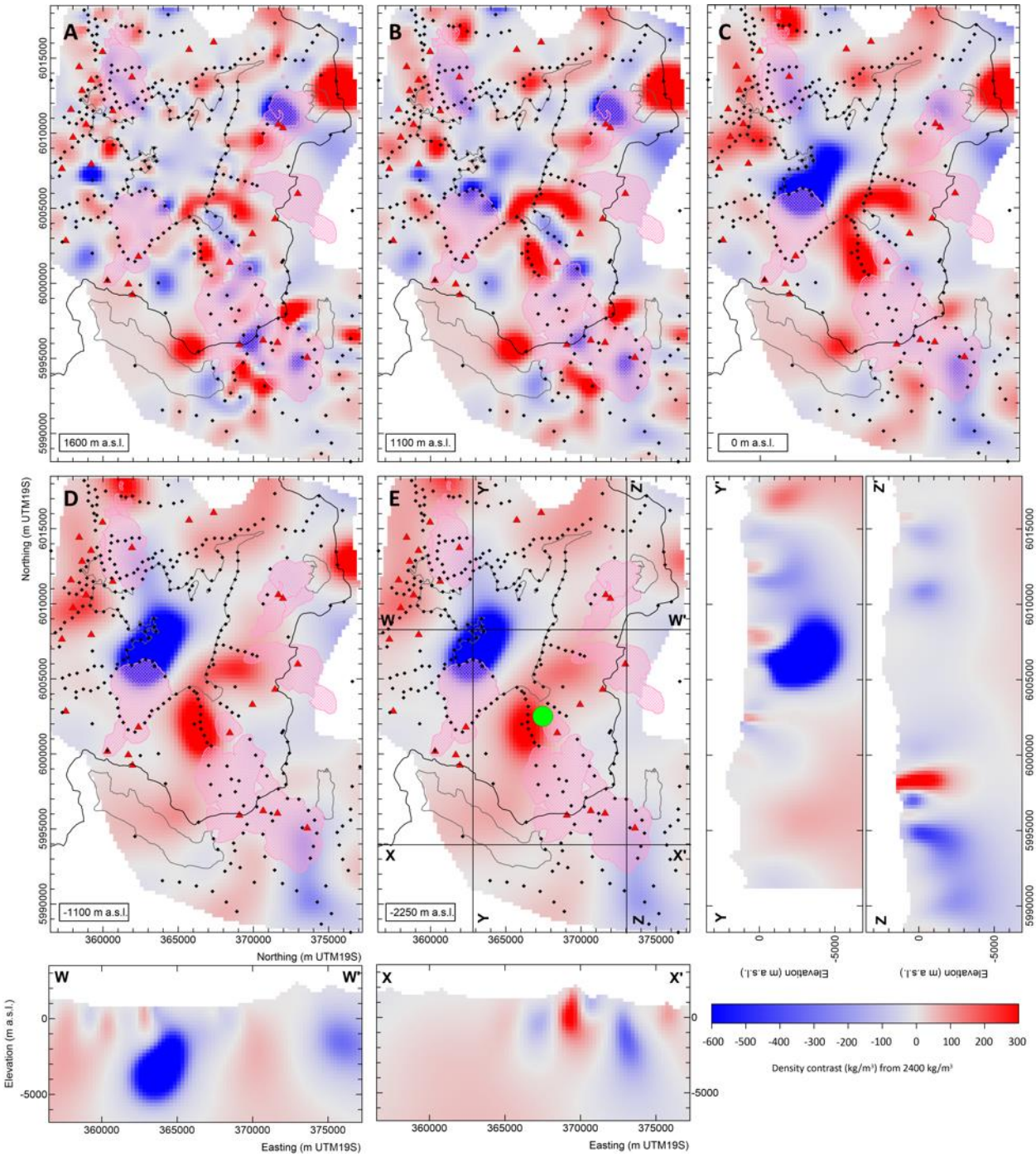

Figure 4. Depth slices and cross sections from the median inverse model. The green dot is the inferred source of shoreline tilting from Singer et al. (2018).

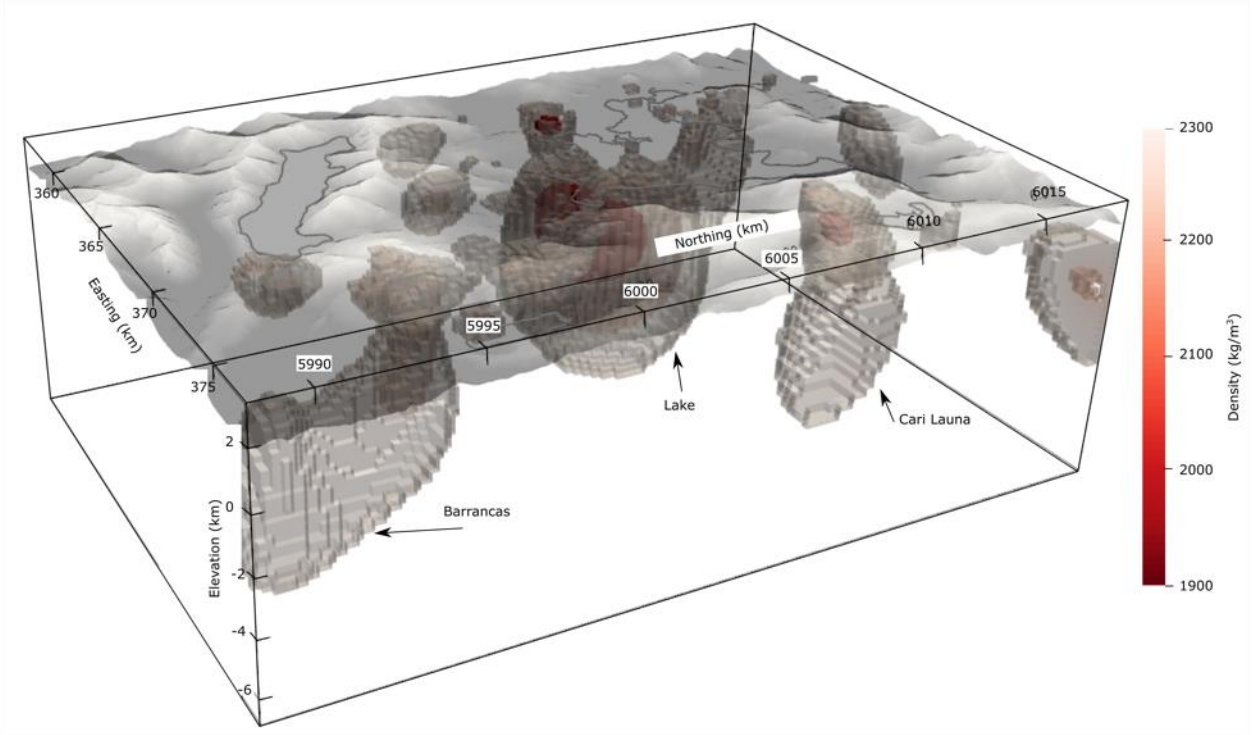

406

407

408 **Figure 5.** Three-dimensional representation of the inverse model showing isosurfaces of <1900 kg/m^3
409 material (red) and 2200-2300 kg/m^3 (grey) material. The Lake low density body is labelled along with the
410 Barrancas and Cari Launa bodies. Other smaller bodies have limited depth extent and likely represent shallow
411 variations in the thicknesses of pyroclastic deposits. The most important of these is the shallow body at the eastern
412 end of Laguna Fea which dams the outlet and poses a flooding hazard should it fail. View is from the south east
413 looking to the north west.

414

415 To assess the probability of a specific density value occurring in a model cell, we ran the
416 inversion with multiple regularization norms that covered the range of smooth, intermediate, and
417 compact models (Fig. 3). From the 10 models, we calculate the probability of a density value
418 occurring in each cell and use this information as a measure of confidence in our model. Figure
419 6 shows the probabilities of modeled densities.

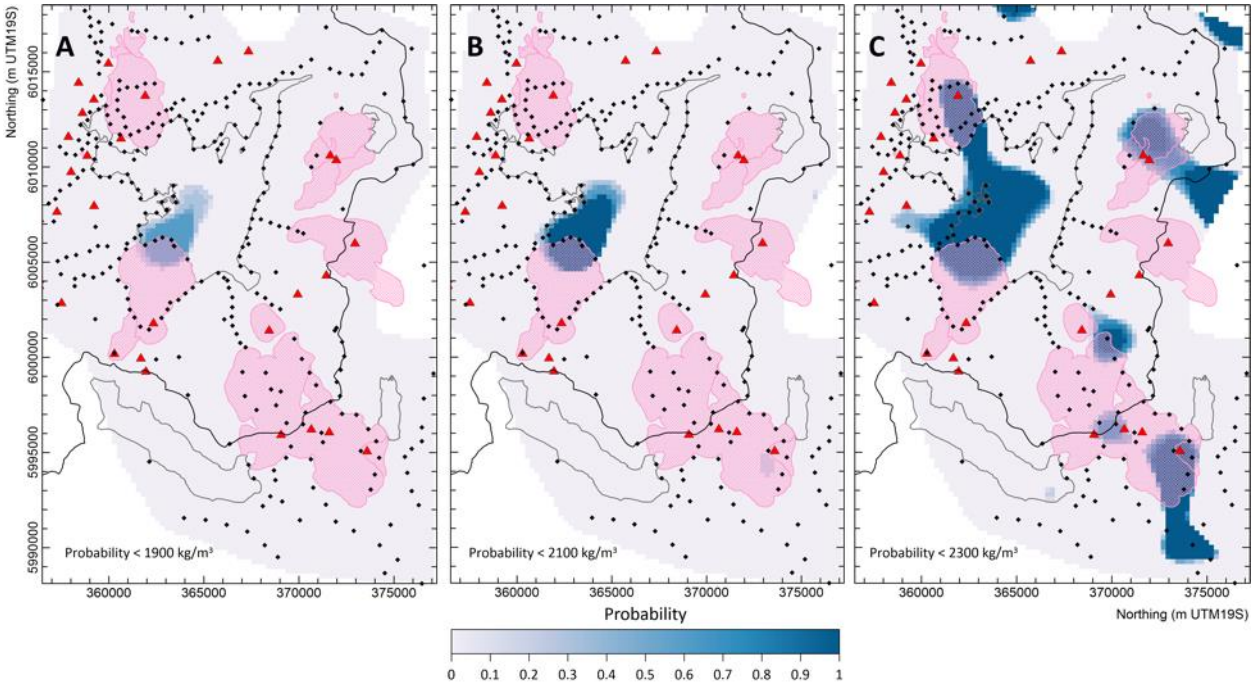

420

421 **Figure 6.** Probability of a density value occurring in the model, A) < 1900 kg/m^3, B)
422 <2100 kg/m^3 and C) <2300 kg/m^3. Depth slice is at 0 m a.s.l. (approximately 2.5 km depth).

423

424 Only the Lake body shows a probability of having a density of <1900 kg/m^3 (p=0.6). We
425 use the probability descriptors of the IPCC (Mastrandrea et al., 2011) to describe this probability
426 as a likely occurrence. The Lake body is virtually certain (p>0.99) to have a density of <2100
427 kg/m^3 (Fig. 6B). None of the models indicate material with density <1900 kg/m^3 beneath
428 Barrancas or Cari Launa. It is unlikely (p=0.2) that material <2100 kg/m^3 exists beneath the
429 Barrancas complex, although it is virtually certain (p>0.99) that material with density 2100 -
430 2300 kg/m^3 occurs under the south-east corner of the Barrancas complex near the *rng* eruption
431 vent. It is also virtually certain (p>0.99) that material with 2100 - 2300 kg/m^3 occurs beneath
432 Cari Launa rhyolite flows in the northeast, although the model is poorly constrained in this
433 location by sparse data coverage.

To test the effect of Bouguer correction density on our residual anomaly data - and hence inversion models - we re-corrected the gravity data with a correction density of 2670 kg/m^3 (see supplementary material). This density is similar to the basement density, but probably too high for unconsolidated volcanic rocks that comprise the Bouguer slab and terrain above the reduction ellipsoid. We subtracted a second-order polynomial regional field to create a new residual gravity anomaly for inversion. Re-running the inversion models with a higher (2670 kg/m^3) terrain density results in density contrasts beneath Barrancas of -300 to -400 kg/m^3, or absolute densities of 2270 to 2370 kg/m^3. In other words, the estimated densities below the Barrancas complex are similar to the densities obtained using the preferred 2400 kg/m^3 correction density. Although derivation of absolute densities from density contrasts beneath the ellipsoid needs to be done with caution, the density values for the anomalous body beneath Barrancas are very likely in the range of 2100 to ~2370 kg/m^3.

6 Discussion

Andersen et al. (2017b; 2018; 2019) and Klug et al. (2020) propose a conceptual model of the LdMVF magma system based on geochronology, whole rock and trace geochemical distinctions, mineral barometry/thermometry, mineral textures, diffusion chronometry, and melt inclusion volatile contents. In this model, the sub-LdMVF magma reservoir exists as an extensive, largely crystalline mush (<15% melt) of probable rhyodacitic composition within which are smaller heterogeneous hot zones of extractable magma (25-50 % melt) that contain discrete pools of eruptible, crystal-poor, rhyolite (>85% melt). Critically, these studies identified two geochemically distinct rhyolite compositions that did not interact with one another; one that erupted during early post-glacial time, (22-19 ka) and another, that includes the Barrancas complex, that erupted during the Holocene. These two distinct rhyolite magmas may reflect

differences in crystal phase proportions in the mush and thermal heterogeneity of the reservoir with hot zones reflecting regions of variable basaltic intrusion (Andersen et al., 2019). We use this conceptual petrological model as a framework to interpret and integrate our geophysical model findings.

To constrain our interpretations of the new gravity anomaly data and inversion model, we used measured densities of rock samples from the exhumed Risco Bayo – Huemul plutonic complex inferred to represent a frozen analog of a silicic melt storage system. We further constrain our interpretations with thermodynamic modeling of dacite and rhyolite melt data to estimate the present-day melt, volatile, and crystal phases beneath the Barrancas complex that last erupted 2 ka. We investigate if valley filling pyroclastic deposits can account for the Barrancas anomaly and briefly discuss the effect of hydrothermal activity on our interpretation. Finally, we discuss the physical interpretation of the density models and implications for magma storage within the LdMVF, in comparison to previously published findings on the LdMVF magma system (Miller et al., 2017b; Andersen et al., 2018; Cordell et al., 2018; Wespestad et al., 2019; Bai et al., 2020; Klug et al., 2020).

Our expanded gravity coverage and updated inversion model reveals with high confidence that the low-density bodies at Barrancas and Cari Launa are discrete from the Lake gravity anomaly. The Lake anomaly has been previously interpreted as caused by a shallow melt rich lens within a broader mush (Miller et al., 2017b; Wespestad et al., 2019; Bai et al., 2020). We focus on the Barrancas anomaly as the Cari Launa anomaly is poorly resolved by our dataset.

The Barrancas gravity low (Fig. 2) partially coincides with a 60 – 120 m thick block and ash flow deposit from the 11.5 ka eruption, which filled the valley south of the edifice (Sruoga et al., 2015; 2018) (Fig. 1). We calculated the gravity effect of the pyroclastic deposit using a

simple two-dimensional model of a 120 m deep, 2 km wide V-shaped valley, filled with material having a density contrast of -400 kg/m^3 which results in a -1.6 mGal anomaly. The absolute density of the valley fill (approximately 2000 kg/m^3) is the same as used to model the shallow infill from the 1.8 ka Taupo caldera eruption (Davy & Caldwell, 1998) and is the same as the average bulk density of 106 samples measured from the 2.36 ka Mt Meagre block and ash flow (Michol et al., 2008). To recreate the magnitude of the observed anomaly requires filling a valley 600 m deep or for the density of the material to be around 900 kg/m^3; both parameters are considered unrealistic. Further, the valley filling model does not reflect the longer wavelengths of the observed anomaly. Therefore, the entire -6 mGal Barrancas anomaly is not solely due to thick low-density pyroclastic material.

A small (> -1 to <1 mGal) anomaly immediately west of the Barrancas anomaly is associated with shallow body of low-density material damming the outlet of Laguna Fea (Fig. 5). This pumice dam is recognized as a significant hazard to communities living downstream (P. Sruoga, pers. comm., 2020). There is no stream outlet from Laguna Fea, and via stream piracy and capture, eventually this pumice dam will likely fail and flood the Barrancas valley.

The 62 m upwarping of the Holocene paleoshoreline is inferred by Singer et al. (2018) to reflect repeated intrusion events below Barrancas. These intrusion events occurred over the last 9.4 ka, at peak rates of 0.04 km^3/year, or an integrated average rate of 0.0023 km^3/year (Singer et al., 2018). Models of conductive heat loss from plutons formed by repeated magma injection (e.g., Blundy & Annen, 2016) show that in small high flux systems - such as LdMVF - there remains significant eruptible melt even 10 ka since the last magma injection. Once the final magma injection ends, it takes 50-100 ka for the system to first cool to a non-eruptible state (< approximately 40 % melt) and to finally solidify. Therefore, combined with the recent (<2 ka)

503 and long-lived eruptive history of the Barrancas complex, we interpret this large low-density
504 body, and the low velocity bodies from seismic tomography, to be remnants of magmatic storage
505 systems that fed the most recent eruptions between 1 and 2 ka. In the following sections we
506 discuss the likely state of the magma beneath the Barrancas complex.

507 **6.1 Implications of plutonic rock equivalents for gravity anomaly interpretation**

508 The 7.2 to 6.0 Ma Risco Bayo - Huemul plutonic complex was emplaced at 3.7 to 7.2 km
509 depth and spans a similar range in rock composition as the LdMVF, including crystal-rich
510 rhyodacites, and the crystal-poor rhyolites that produced the entire Barrancas complex (Schaen et
511 al., 2017; 2018). Thus, the Risco Bayo and Huemul plutonic rocks provide analogues for
512 portions of the magma reservoir underlying the LdMVF.

513 Relative to metamorphosed basement rocks, granites commonly yield negative Bouguer
514 anomalies (e.g., Cordell et al., 1985; Gaynor et al., 2019) if the Bouguer correction (i.e.,
515 surrounding crustal) density is approximately 2600-2700 kg/m^3. Metamorphosed basement
516 rocks in the Chilean Central Andes near Laguna del Maule are typically at 2-3 km depth (Godoy
517 et al., 1999) and have densities of approximately 2700 kg/m^3. Overlying these basement rocks
518 are sedimentary and volcanic rock packages of density between 2300 and 2600 kg/m^3, consistent
519 with the correction density obtained for the Laguna del Maule and Barrancas area of 2400 kg/m^3.
520 If frozen plutonic bodies of similar composition and density to the Risco Bayo and Huemul
521 plutons were present at shallow depth (2-3 km) beneath Barrancas, they would create a small
522 positive Bouguer anomaly, relative to our correction density of 2400 kg/m^3. If the density of the
523 crust increases with depth, then these granites would produce neutral or negative anomalies.

524 The lowest density rocks of the exhumed Risco Bayo and Huemul plutonic complex that
525 represent “frozen melt” have an average density of 2439±15 kg/m^3 (section 2.1) similar to the

Bouguer correction density. This density is higher than the density values returned by the inversion model for the body beneath the Barrancas complex (2180 kg/m^3) and suggests that the Barrancas body cannot be a cold, solidified pluton. Rather, it may contain some percent melt and perhaps an exsolved volatile phase, as also inferred from the slowing of seismic waves through this region (Wespestad et al., 2019, Bai et al., 2020), and the high H_2O contents of the rhyolitic melts (Klug et al., 2020). We therefore propose that the low-density body beneath the Barrancas complex is a combination of low-density surface lavas and pyroclastic material, and a deeper remnant magma storage system that contains some proportion of residual melt left over from the last eruption at 1-2 ka. We investigate this hypothesis in the following section using MELTS thermodynamic modelling tool.

6.2 Thermodynamic models and density anomalies

Our gravity model of the Barrancas complex - constrained by independent density measurements, cooling models, and seismic tomography evidence - suggests that a melt phase is present in the storage system at 3-4 km depth. To further investigate the presence of melt or fluid phases within the modeled low-density body beneath the Barrancas complex, we use Rhyolite MELTS for Excel (Gualda & Ghiorso, 2015) to construct phase diagrams that relate magma density (melt, crystal, and fluid phases) to temperature and pressure. The magma body is assumed to be a crystal-rich mush of andesitic to dacitic bulk composition, which contains volumetrically minor interstitial rhyodacitic to rhyolitic melt. Within the relatively cool upper crust, this is a more likely state for long-term storage and incubation of silicic magma than a large, long-lived body of rhyolitic melt (Cooper & Kent, 2014; Andersen et al., 2018). Andersen et al. (2018) show that for a dacite magma at 200 MPa (ca. 8 km depth), using the external volatile flux model, a density of 2200-2300 kg/m^3 can be produced with less than 10% exsolved

549 fluid volume fraction at a temperature of around 750°C. This is consistent with the high H_2O
550 content of melt inclusions and volatile saturation of most rhyolite erupted within the LdMVF
551 (Klug et al., 2020). However, unlike these rhyolites the Barrancas domes show evidence of
552 hydrothermal alteration and collapse to produce a large pyroclastic flow, in which melt
553 inclusions contain little CO_2 and low H_2O contents (Klug et al., 2020). These features are
554 interpreted by Klug et al. (2020) to reflect much shallower emplacement (50-100 MPa; less than
555 4 km depth) and extensive degassing of rhyolitic magma prior to eruption.

556 To model the densities of residual magmas that equilibrate at low pressures and lose
557 volatiles, simulating conditions thought to occur beneath the Barrancas complex, we use the
558 rhyodacite of Laguna sin Puerto containing 69% silica, 2.5% H_2O and no CO_2 (Hildreth et al.,
559 2010; Klug et al., 2020) as a starting composition. We normalize the composition to retain the
560 H_2O phase within the melt and then cool the magma to its solidus at a constant pressure of 110
561 MPa. The modeled values allow us to track density changes as the magma cools and crystallizes
562 (Fig. 7A). The liquidus is ~960 °C (not shown on the plot) and as cooling occurs the magma
563 density rises to a peak of 2420 kg/m^3 at 762 °C. At these conditions, quartz begins to crystallize
564 and at 760 °C the H_2O begins to exsolve, lowering the density. Between 744 and 742 °C, with
565 40 % melt remaining, the exsolved fluid phase doubles in mass from 0.64 to 1.31 wt. % at which
566 point the density drops further. The density range of Barrancas gravity models span from 2200 -
567 2350 kg/m^3 matching conditions that include the solidus and up to ~30 % melt plus exsolved
568 H_2O (Fig. 7A). In contrast, Figure 7B shows the total system densities of a LdMVF rhyolite
569 containing 5 wt. % H_2O at 90 and 110 MPa, with the expected pressure at the approximate depth
570 range (2.5-3.5 km) of the Lake body imaged by the gravity inversion and teleseismic
571 tomography. Five weight % H_2O is likely a minimum, as melt inclusions contain up to 8 wt.%

572 H_2O (Klug et al., 2020) that would further lower the density. The latter MELTS model replicates
573 the densities recovered by the gravity inversion for the Lake anomaly (1800 to 1900 kg/m^3). To
574 reproduce the model densities required for Lake anomaly, the magma system must contain an
575 exsolved fluid phase, although the proportion of melt is less certain. A lower bound of 5-14 %
576 melt is obtained by coarser gridded seismic tomography models (Wespestad et al., 2019, Bai et
577 al., 2020), while the closer spaced gravity data suggests small pockets with ~50 % melt is
578 possible in parts of the system depending on the pressure.

579

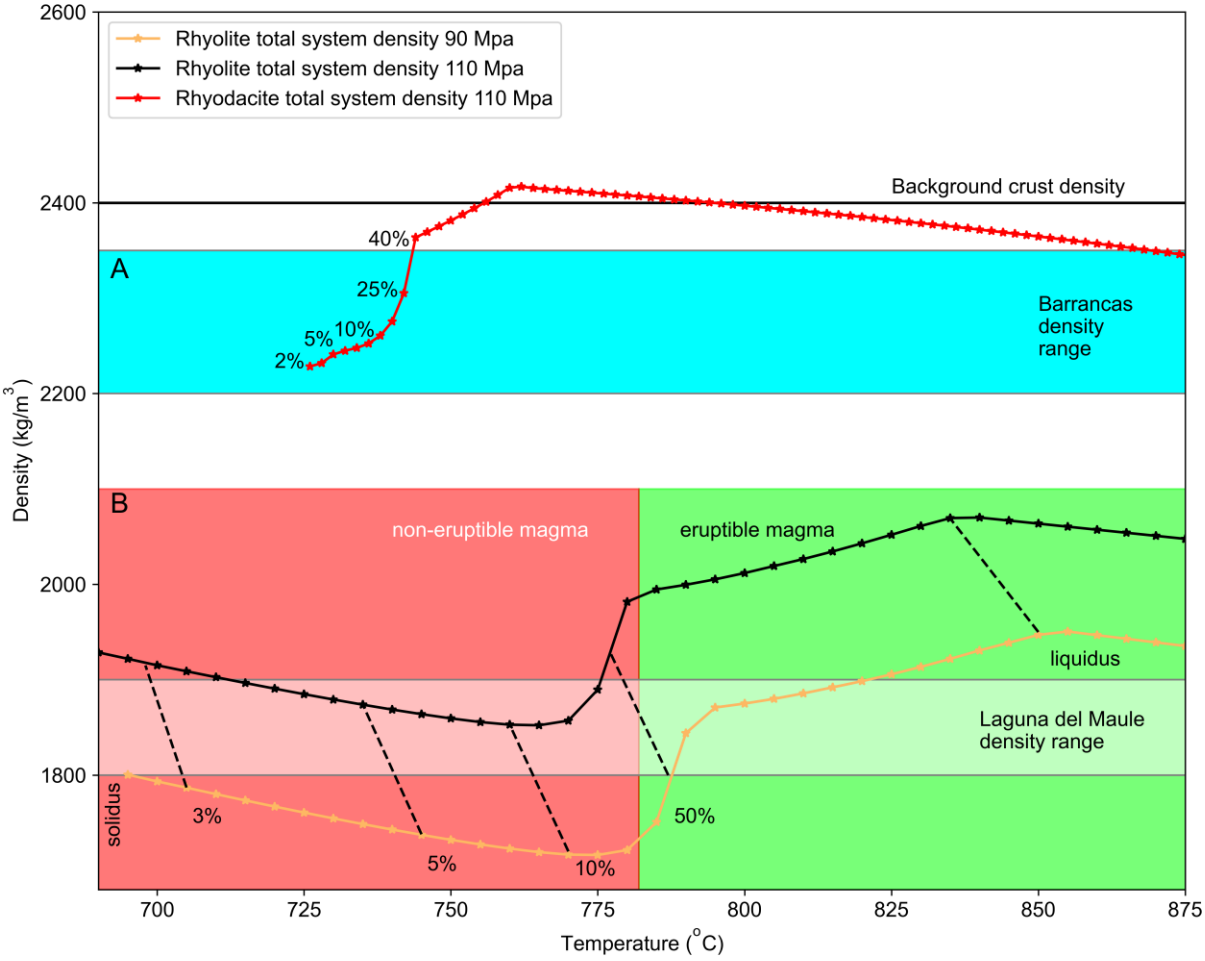

580

581 **Figure 7.** Plots of density as a function of temperature estimated by rhyolite MELTS simulations. In both plots the
582 annotated percentages indicate melt percent. A) Total system densities (crystal, melt, volatile) of rhyodacite magma

583 containing 2.5% H_2O (red). The range of densities from the gravity inversion model at Barrancas are shaded light
584 blue. B) Total system densities of rhyolite magma at 90 and 110 MPa (approx. 2.5 to 4.5 km depth) with melt
585 proportions (dashed lines). The range of densities from the inversion model of the Lake anomaly are shaded grey.
586 Eruptible versus non-eruptible magma is shaded red and green around the approximately 50 melt percent
587 temperature.

588 ### 6.3 Effect of hydrothermal activity

589 Miller et al. (2017a) proposed that gravity changes associated with the Lake anomaly in
590 the top 2 km are caused by the influx of hydrothermal fluids into the Troncoso fault zone. As
591 our modelled low-density bodies extend close to the surface, we consider whether the top portion
592 of these bodies may in fact represent a rock hosted hydrothermal system as suggested by
593 Andersen et al. (2018) to explain in part the low densities observed. In a liquid-dominated
594 hydrothermal system within a porous rock, pore space initially filled by air is replaced by brine
595 resulting in a small gravity increase. Hence, the presence of an active liquid-dominated
596 hydrothermal system would slightly increase the observed gravity relative to the surrounding
597 area.

598 The Barrancas domes show widespread evidence for advanced argillic alteration caused
599 by circulation of > 300° C fluids during the Holocene (Sruoga et al., 2015). Hydrothermal
600 alteration can often lower the density of rock (e.g., Miller & Williams-Jones, 2016), although the
601 magnitude of the density decrease from alteration is typically 1-2 mGal and not enough to
602 explain the gravity lows observed. MT models of the Barrancas area (Cordell et al., 2018) show
603 a small shallow (1-2 km) conductive anomaly (10 Ωm) near the summit of Barrancas that may be
604 consistent with conductive clay minerals formed by hydrothermal alteration. However, the
605 gravity anomaly extends far south from the altered domes. As such, hydrothermal alteration is
606 likely to play only a minor part in the observed gravity anomaly.

607 **6.4 Present state of the Barrancas and broader Laguna del Maule magma reservoir**

608 Our interpretation of the density model of the LdMVF is partially constrained by
609 equivalent plutonic rocks from the nearby Risco Bayo – Huemul pluton that represent a "frozen"
610 analog. These rocks have densities > 2400 kg/m^3, which would result in positive gravity
611 anomalies if they existed in our residual anomaly map. We note that positive gravity anomalies
612 exist in the older, northern part of the volcanic field suggesting they may represent the cold,
613 frozen portions that may have become plutons. A ridge of positive gravity anomaly divides the
614 Lake anomaly from the Barrancas anomaly. The inversion model indicates that this ridge is a
615 shallow feature extending towards the surface and may represent a buried sequence of Pliocene
616 andesitic lavas comprising the Cola de Zorro Formation within the uppermost 2 km (Hildreth et
617 al., 2010), as opposed to a frozen pluton.

618 Our new density model of the broader LdMVF has captured what we interpret as at least
619 two magma bodies at different stages of maturity. The large low-density body beneath the Lake
620 represents an active melt storage system containing a substantial free volatile phase, driven by
621 deeper injection of basalt, supplying heat and volatiles and propelling the present-day uplift (Le
622 Mével et al., 2016; Zhan et al., 2019; Klug et al., 2020). The depth of the reservoir is consistent
623 with melt inclusion derived pressure estimates (Klug et al., 2020) and suggests that gravity is
624 imaging the top portion of a trans-crustal magmatic system that extends to >25 km depth
625 (Andersen et al., 2017b; Cordell et al., 2018; Bai et al., 2020). The geochemical data indicate
626 spatially and petrologically discrete magma bodies have persisted during at least the last 25 ka,
627 producing rhyolite eruptions. This data suggest that the multiple discrete bodies captured in the
628 present-day geophysical models are the norm, rather than the exception, at the LdMVF.

629 Given the spatial coincidence of the teleseismic low-Vp anomaly and the Lake gravity
630 anomaly, joint inversion of the two, either via structural gradients or by analytic relationships

631 that link Vp and density, is likely to yield greater insight into the physical properties of this
632 magma body, with ramifications for its present state and future trajectory.

633 The newly discovered Barrancas magma body represents the still warm remains of a
634 magma body within the reservoir that last erupted 1-2 ka. The melt content is uncertain, but it is
635 likely to be < 30 %; further, it may contain <2.5% volatile phase and is thus in a non-eruptible
636 condition. This interpretation is consistent with the low H_2O and CO_2 contents and low
637 emplacement pressures (50 – 100 MPa) from melt inclusions in the 11.5 ka Barrancas pyroclastic
638 flow deposit (Klug et al., 2020), suggesting that the magma was thoroughly outgassed prior to its
639 endogenous and exogenous emplacement as a dome complex at very shallow depths. The Melts
640 models also suggest that the Barrancas magma body could be at solidus temperatures. However,
641 the surface wave and teleseismic tomography (Wespestad et al., 2019; Bai et al., 2020)
642 anomalies - although on the edge of the seismic array - imply some degree of melt remains. Melt
643 contents inferred by teleseismic tomography suggests the body beneath Barrancas volcanic field,
644 by comparison to the Lake low VP anomaly, has < 14 % melt. The deeper portion of the low-
645 density body under Barrancas may represent the cooling, volatile-depleted, cumulate framework
646 of a dacitic magma body, which was once the "warm storage" source of rhyolite melt (Anderson
647 et al., 2017).

648 One possible end point in the development of the Barrancas magma is the formation of a
649 high silica pluton, similar to the exhumed Huemul pluton to the west of the LdMVF. However,
650 future injection of basalt beneath the Barrancas complex, as is postulated to be occurring beneath
651 the Lake anomaly, could reactivate this magma body and continue to drive the paleoshoreline
652 upwarping observed since 9.4 ka. This scenario is supported by petrochronologic evidence from
653 the Barrancas complex (Andersen et al., 2019), which suggests that the erupted rhyolites were

654 sourced from a long lived "warm" part of the magma reservoir. This magma reservoir
655 experienced external additions of heat and volatiles that remobilized interstitial melt shortly prior
656 to successive eruptions.

657 **7 Conclusions**

658 The new residual gravity anomaly map of the LdMVF shows a -6 mGal gravity low
659 extending from the summit of the Barrancas complex to 5 km southeast of the summit at depth.
660 The inversion model of the Barrancas anomaly shows a 64 km^3 body dipping to the south east at
661 a depth of 2-4 km (sea level to 2 km below sea level) with a modelled density of ~2200 to 2350
662 kg/m^3. Our interpretation - guided by measured densities from the nearby Risco Bayo - Huemul
663 plutonic rocks, thermodynamic modeling, and petrologic observations - is that the Barrancas low
664 density body represents a volatile poor magma with a <30 % melt proportion. This interpretation
665 is consistent with the presence of magma that degassed at depths less than 3-4 km and produced
666 domes comprising the Barrancas volcanic complex. We propose this magma represents the
667 cooling remnant of a once active melt pocket that last erupted 1-2 ka. Moreover, the growth of
668 this magma reservoir in the shallow crust is likely responsible for the >60 m uplift of the
669 paleoshoreline in the southern part of the LDM basin since 9.4 ka.

670 Our new geophysical observations of the location, geometry, and state of the magmatic
671 anomalies in the SE basin provide geophysical evidence that integrates with petrological models
672 of melt storage. The Barrancas gravity anomaly represents a rhyodacite melt stored in the
673 shallow crust in warm zones that can be melted, differentiated, extracted, and erupted.
674 Thermodynamic modelling shows that these bodies may transition from moribund to melt rich
675 over a relatively small temperature range. Such as temperature increase could result from basalt

intrusion, proposed as a mechanism for the present-day inflation above the Lake anomaly (e.g., Le Mével et al., 2016).

The new gravity model of the LdMVF corroborates extensive petrologic findings and provides geophysical evidence for at least two separate magma bodies within the same volcanic field. The emerging picture is one in which a broader magma reservoir can coevally host multiple melt-bearing domains in differing physical states. This finding has important implications for future hazard monitoring of the LdMVF, in both Chile and Argentina, as the Barrancas complex straddles this border.

Acknowledgements

The Barrancas volcanic field is located at the crest of the Andes, on the border of Argentina and Chile. Sebastian Garcia and Alvaro Amigo were critical in working with their respective governments to allow us to complete this fieldwork; and Felipe Diaz acted as the liaison of the helicopter company with the government agencies. Our sincere thanks to all of them. Peter Sobol provided logistical support in the field. We gratefully acknowledge the patience and tenacity of field assistants Eve Meltzer, Jake Klug, and Claire Ruggles. Thanks to Nicolas Garibaldi for providing samples of the Risco Bayo and Huemul plutons and to Luis Torres for accommodation and support in Chile. Emily Mixon provided help with the Melts model work. Kurt Feigl provided funds from his portion of LdM funding for the helicopter time that allowed the fieldwork to happen. We thank the entire Laguna del Maule research team for thoughtful and constructive conversations that contributed to this paper. Gravity data are available from https://figshare.com/articles/Gravity_data_from_Laguna_del_Maule/12479981. This study was supported by NSF grant EAR-1411779. Craig Miller is supported by New

Zealand government, Ministry of Business, Innovation and Employment, SSIF funding, under the Volcano Hazards and New Zealand Geothermal programs.

Author Contributions

ST coordinated and participated in data collection, processing, and analysis of the Barrancas dataset. CM ran the inversion models and led the analysis and writing of the manuscript. BT conceived the project, organized the fieldwork, and participated in field work in Chile and Argentina, and assisted in data processing and analysis. DF ran the synthetic model and provided the code for the inversion models. BSS initiated the integrative study of Laguna del Maule, obtained the funding, established a collaboration with SERNAGEOMIN, facilitated permission for the helicopter work in the border area, and provided the petrologic context. All authors provided critical review and editing of the final manuscript.

References

Andersen, N. L., Jicha, B. R., Singer, B. S., & Hildreth, W. (2017a). Incremental heating of Bishop Tuff sanidine reveals preeruptive radiogenic Ar and rapid remobilization from cold storage. *Proceedings of the National Academy of Sciences*, 201709581. https://doi.org/10.1073/pnas.1709581114

Andersen, N. L., Singer, B. S., Jicha, B. R., Beard, B. L., Johnson, C. M., & Licciardi, J. M. (2017b). Pleistocene to Holocene Growth of a Large Upper Crustal Rhyolitic Magma Reservoir beneath the Active Laguna del Maule Volcanic Field, Central Chile. *Journal of Petrology*, *58*(1), 85–114. https://doi.org/10.1093/petrology/egx006

Andersen, N. L., Singer, B. S., Costa, F., Fournelle, J., Herrin, J. S., & Fabbro, G. N. (2018).

Petrochronologic perspective on rhyolite volcano unrest at Laguna del. *Earth and Planetary Science Letters*, *493*, 57–70. https://doi.org/10.1016/j.epsl.2018.03.043

Andersen, N. L., Singer, B. S., & Coble, M. A. (2019). Repeated Rhyolite Eruption From Heterogeneous Hot Zones Embedded Within a Cool, Shallow Magma Reservoir. *Journal of Geophysical Research: Solid Earth*, *124*(3), 2582–2600. https://doi.org/10.1029/2018JB016418

Bachmann, O., Miller, C. F., & de Silva, S. L. (2007). The volcanic-plutonic connection as a stage for understanding crustal magmatism. *Journal of Volcanology and Geothermal Research*, *167*(1–4), 1–23. https://doi.org/10.1016/j.jvolgeores.2007.08.002

Bachmann, Olivier, & Bergantz, G. (2008). The magma reservoirs that feed supereruptions. *Elements*, *4*(1), 17–21. https://doi.org/10.2113/GSELEMENTS.4.1.17

Bai, T., Thurber, C., Lanza, F., Singer, B. S., Bennington, N., Keranen, K., & Cardona, C. (2020). Teleseismic tomography of the Laguna del Maule Volcanic Field in Chile. *Journal of Geophysical Research: Solid Earth*. https://doi.org/10.1029/2020JB019449

Barboni, M., Boehnke, P., Schmitt, A. K., Mark Harrison, T., Shane, P., Bouvier, A. S., & Baumgartner, L. (2016). Warm storage for arc magmas. *Proceedings of the National Academy of Sciences of the United States of America*, *113*(49), 13959–13964. https://doi.org/10.1073/pnas.1616129113

Battaglia, M., Poland, M. P., & Kauahikaua, J. (2012). GTools: An interactive computer program to process gravity data for high resolution applications. In *AGU Fall Meeting* (pp. GP43B-1143).

Bertrand, E. A., Caldwell, T. G., Hill, G. J., Wallin, E. L., Bennie, S. L., Cozens, N., et al.

(2012). Magnetotelluric imaging of upper-crustal convection plumes beneath the Taupo Volcanic Zone, New Zealand. *Geophysical Research Letters*, *39*(2), 1–6. https://doi.org/10.1029/2011GL050177

Blundy, J. D., & Annen, C. J. (2016). Crustal Magmatic Systems from the Perspective of Heat Transfer. *Elements*, *12*(2), 115–120. https://doi.org/10.2113/gselements.12.2.115

Brocher, T. M. (2005). Empirical Relations between Elastic Wavespeeds and Density in the Earth's Crust. *Bulletin of the Seismological Society of America*, *95*(6), 2081–2092. https://doi.org/10.1785/0120050077

Cáceres, F., Castruccio, Á., & Parada, M. A. (2018). Morphology, Effusion Rates, and Petrology of Postglacial Lavas of Laguna del Maule Volcanic Field, Chilean Andes, and Implications for Their Plumbing System. *Geochemistry, Geophysics, Geosystems*, *19*(12), 4925–4944. https://doi.org/10.1029/2018GC007817

Cockett, R., Kang, S., Heagy, L. J., Pidlisecky, A., & Oldenburg, D. W. (2015). SimPEG: An open source framework for simulation and gradient based parameter estimation in geophysical applications. *Computers and Geosciences*, *85*, 142–154. https://doi.org/10.1016/j.cageo.2015.09.015

Comeau, M. J., Unsworth, M. J., Ticona, F., & Sunagua, M. (2015). Magnetotelluric images of magma distribution beneath Volcán Uturuncu, Bolivia: Implications for magma dynamics. *Geology*, *43*(3), 243–246. https://doi.org/10.1130/G36258.1

Cooper, K. M., & Kent, A. J. R. (2014). Rapid remobilization of magmatic crystals kept in cold storage. *Nature*, *506*(7489), 480–483. https://doi.org/10.1038/nature12991

Cordell, D., Unsworth, M. J., & Díaz, D. (2018). Imaging the Laguna del Maule Volcanic Field,

766 central Chile using magnetotellurics: Evidence for crustal melt regions laterally-offset from
767 surface vents and lava flows. *Earth and Planetary Science Letters*, *488*, 168–180.
768 https://doi.org/10.1016/j.epsl.2018.01.007

769 Cordell, D., Unsworth, M. J., Diaz, D., Reyes-Wagner, V., Currie, C. A., Hicks, S. P.(2019)
770 Fluid and melt pathways in the central Chilean subduction zone near the 2010 Maule
771 earthquake (35–36°S) as inferred from magnetotelluric data. *Geochemistry, Geophysics,*
772 *Geosystems 20*(4), 1818-1835.

773 Cordell, D., Unsworth, M. J., Lee, B., Diaz, D., Bennington, N. (2020) Integrating
774 magnetotelluric and seismic images of silicic magma systems: A case study from the
775 Laguna del Maule Volcanic Field, central Chile. *Journal of Geophysical Research: Solid*
776 *Earth.*

777 Cordell, L., Long, C. L., & Jones, D. W. (1985). Geophysical expression of the batholith beneath
778 Questa Caldera, New Mexico. *Journal of Geophysical Research*, *90*(4), 11263.
779 https://doi.org/10.1029/JB090iB13p11263

780 Davy, B. W., & Caldwell, T. G. (1998). Gravity, magnetic and seismic surveys of the caldera
781 complex, Lake Taupo, North Island, New Zealand. *Journal of Volcanology and Geothermal*
782 *Research*, *81*, 69–89. https://doi.org/10.1016/S0377-0273(97)00074-7

783 Druitt, T. H., Costa, F., Deloule, E., Dungan, M., & Scaillet, B. (2012). Decadal to monthly
784 timescales of magma transfer and reservoir growth at a caldera volcano. *Nature*, *482*(7383),
785 77–80. https://doi.org/10.1038/nature10706

786 Feigl, K. L., Le Mevel, H., Tabrez Ali, S., Cordova, L., Andersen, N. L., DeMets, C., & Singer,
787 B. S. (2014). Rapid uplift in Laguna del Maule volcanic field of the Andean Southern
788 Volcanic zone (Chile) 2007-2012. *Geophysical Journal International*, *196*(2), 885–901.

https://doi.org/10.1093/gji/ggt438

Folguera, A., Alasonati Tašárová, Z., Götze, H.-J., Rojas Vera, E., Giménez, M., & Ramos, V. a. (2012). Retroarc extension in the last 6 Ma in the South-Central Andes (36°S–40°S) evaluated through a 3-D gravity modelling. *Journal of South American Earth Sciences*, *40*, 23–37. https://doi.org/10.1016/j.jsames.2012.08.003

Garibaldi, N., Tikoff, B., Schaen, A. J., & Singer, B. S. (2018). Interpreting Granitic Fabrics in Terms of Rhyolitic Melt Segregation, Accumulation, and Escape Via Tectonic Filter Pressing in the Huemul Pluton, Chile. *Journal of Geophysical Research: Solid Earth*. https://doi.org/10.1029/2018JB016282

Gaynor, S. P., Coleman, D. S., Rosera, J. M., & Tappa, M. J. (2019). Geochronology of a Bouguer Gravity Low. *Journal of Geophysical Research: Solid Earth*, *124*(3), 2457–2468. https://doi.org/10.1029/2018JB015923

Glazner, A. F., Bartley, J. M., Coleman, D. S., Gray, W., & Taylor, R. Z. (2004). Are plutons assembled over millions of years by amalgamation from small magma chambers? *GSA Today*, *14*(4), 4. https://doi.org/10.1130/1052-5173(2004)014<0004:APAOMO>2.0.CO;2

Godoy, E., Yañez, G., & Vera, E. (1999). Inversion of an Oligocene volcano-tectonic basin and uplifting of its superimposed Miocene magmatic arc in the Chilean Central Andes: First seismic and gravity evidences. *Tectonophysics*, *306*(2), 217–236. https://doi.org/10.1016/S0040-1951(99)00046-3

Gualda, G. A. R., & Ghiorso, M. S. (2015). MELTS_Excel: A Microsoft Excel-based MELTS interface for research and teaching of magma properties and evolution. *Geochemistry,Geophysics,Geosystems*, *16*, 315–324.

https://doi.org/10.1002/2014GC005545.Received

Hildreth, W., Godoy, E., Fierstein, J., & Singer, B. S. (2010). Laguna del Maule volcanic field: Eruptive history of a Quaternary basalt to rhyolite distributed volcanic field on the Andean range crest in central Chile. *Servicio Nacional de Geologia y Mineria, Bolletin*, *63*, 145.

Hinze, W. J., Aiken, C., Brozena, J., Coakley, B., Dater, D., Flanagan, G., et al. (2005). New standards for reducing gravity data: The North American gravity database. *GEOPHYSICS*, *70*(4), J25–J32. https://doi.org/10.1190/1.1988183

Huber, C., Townsend, M., Degruyter, W., & Bachmann, O. (2019). Optimal depth of subvolcanic magma chamber growth controlled by volatiles and crust rheology. *Nature Geoscience*. https://doi.org/10.1038/s41561-019-0415-6

Klug, J. D., Singer, B. S., Kita, N. T., & Spicuzza, M. J. (2020). Storage and evolution of Laguna del Maule rhyolites: insight from volatile and trace element contents in melt inclusions. *Journal of Geophysical Research: Solid Earth*. https://doi.org/10.1029/2020JB019475

Le Mével, H., Feigl, K. L., Cordova, L., Demets, C., & Lundgren, P. (2015). Evolution of unrest at Laguna del Maule volcanic field (Chile) from InSAR and GPS measurements , 2003 to 2014. *Geophysical Research Letters*, 1–24. https://doi.org/10.1109/36.662741.Pitz

Le Mével, H., Gregg, P. M., & Feigl, K. L. (2016). Magma injection into a long-lived reservoir to explain geodetically measured uplift: Application to the 2007-2014 unrest episode at Laguna del Maule volcanic field, Chile. *Journal of Geophysical Research: Solid Earth*, *121*(8), 6092–6108. https://doi.org/10.1002/2016JB013066

Le Mével, H., Feigl, K. L., Cordova, L., Bekaert, D.P., & Singer, B.S. (2019) Re-acellerating deformation at Laguna del Maule volcanic field, Southern Andes. *American Geophysical*

Union Fall Meeting Abstracts, 2019AGUFM.G33C0701L

Magee, C., Stevenson, C. T. E., Ebmeier, S. K., Keir, D., Hammond, J. O. S., Gottsmann, J. H., et al. (2018). Magma Plumbing Systems: A Geophysical Perspective. *Journal of Petrology*, (July), 1–35. https://doi.org/10.1093/petrology/egy064

Mastrandrea, M. D., Mach, K. J., Plattner, G. K., Edenhofer, O., Stocker, T. F., Field, C. B., et al. (2011). The IPCC AR5 guidance note on consistent treatment of uncertainties: A common approach across the working groups. *Climatic Change*, *108*(4), 675–691. https://doi.org/10.1007/s10584-011-0178-6

Michol, K. A., Russell, J. K., & Andrews, G. D. M. (2008). Welded block and ash flow deposits from Mount Meager, British Columbia, Canada. *Journal of Volcanology and Geothermal Research*, *169*(3–4), 121–144. https://doi.org/10.1016/j.jvolgeores.2007.08.010

Miller, Craig A, & Williams-Jones, G. (2016). Internal structure and volcanic hazard potential of Mt Tongariro, New Zealand, from 3D gravity and magnetic models. *Journal of Volcanology and Geothermal Research*, *319*, 12–28. https://doi.org/10.1016/j.jvolgeores.2016.03.012

Miller, C. A., Le Mével, H., Currenti, G., Williams-Jones, G., & Tikoff, B. (2017a). Microgravity changes at the Laguna del Maule volcanic field: Magma-induced stress changes facilitate mass addition. *Journal of Geophysical Research: Solid Earth*, *122*(4), 3179–3196. https://doi.org/10.1002/2017JB014048

Miller, Craig A., Williams-Jones, G., Fournier, D., & Witter, J. (2017b). 3D gravity inversion and thermodynamic modelling reveal properties of shallow silicic magma reservoir beneath Laguna del Maule, Chile. *Earth and Planetary Science Letters*, *459*, 14–27. https://doi.org/10.1016/j.epsl.2016.11.007

Nettleton, L. L. (1939). Determination of density for reduction of gravimeter observations. *Geophysics*, *4*(3). https://doi.org/10.1190/1.1437088

Parasnis, D. S. (1966). *Mining Geophysics*. Elsevier, Amsterdam-London-New York.

Paulatto, M., Moorkamp, M., Hautmann, S., Hooft, E., Morgan, J. V., & Sparks, R. S. J. (2019). Vertically Extensive Magma Reservoir Revealed From Joint Inversion and Quantitative Interpretation of Seismic and Gravity Data. *Journal of Geophysical Research: Solid Earth*, *124*(11), 11170–11191. https://doi.org/10.1029/2019JB018476

Peterson, D., Garibaldi, N., Keranen, K., Tikoff, B., Miller, C., Lara, L. E., et al. (2020). Active normal faulting, diking, and doming above the rapidly inflating Laguna del Maule volcanic field, Chile imaged with CHIRP, magnetic, and focal mechanism data. *Journal of Geophysical Research: Solid Earth*. https://doi.org/10.1029/2019JB019329

del Potro, R., Díez, M., Blundy, J., Camacho, A. G., & Gottsmann, J. (2013). Diapiric ascent of silicic magma beneath the Bolivian Altiplano. *Geophysical Research Letters*, *40*(10), 2044–2048. https://doi.org/10.1002/grl.50493

Pritchard, M. E., & Gregg, P. M. (2016). Geophysical Evidence for Silicic Crustal Melt in the Continents: Where, What Kind, and How Much? *Elements*, *12*(2), 121–127. https://doi.org/10.2113/gselements.12.2.121

Represas, P., Catalão, J., Montesinos, F. G., Madeira, J., Mata, J., Antunes, C., & Moreira, M. (2012). Constraints on the structure of Maio Island (Cape Verde) by a three-dimensional gravity model: imaging partially exhumed magma chambers. *Geophysical Journal International*, *190*(2), 931–940. https://doi.org/10.1111/j.1365-246X.2012.05536.x

Rubin, A. E., Cooper, K. M., Till, C. B., Kent, A. J. R., Costa, F., Bose, M., et al. (2017). Rapid

877 cooling and cold storage in a silicic magma reservoir recorded in individual crystals.
878 *Science*, *1156*(June), 1154–1156. https://doi.org/10.1126/science.aam8720

879 Schaen, A. J., Cottle, J. M., Singer, B. S., Brenhin Keller, C., Garibaldi, N., & Schoene, B.
880 (2017). Complementary crystal accumulation and rhyolite melt segregation in a late
881 Miocene Andean pluton. *Geology*, *45*(9), 835–838. https://doi.org/10.1130/G39167.1

882 Schaen, A. J., Singer, B. S., Cottle, J. M., Garibaldi, N., Schoene, B., Satkoski, A. M., &
883 Fournelle, J. (2018). Textural and Mineralogical Record of Low Pressure Melt Extraction
884 and Silicic Cumulate Formation in the late Miocene Risco Bayo-Huemul Plutonic Complex,
885 Southern Andes. *Journal of Petrology*, *59*(10), 1991–2016.
886 https://doi.org/10.1093/petrology/egy087

887 Singer, B S, Andersen, N. L., Le Mével, H., Feigl, K. L., DeMets, C., Tikoff, B., et al. (2014).
888 Dynamics of a large, restless, rhyolitic magma system at Laguna del Maule, southern
889 Andes, Chile. *GSA Today*. https://doi.org/10.1130/GSATG216A.1

890 Singer, B.S., Le Mével, H., Licciardi, J.M., Córdova, L., Tikoff, B., Garibaldi, N., Andersen,
891 N.L., Diefenbach, A.K. & Feigl, K.L. (2018). Geomorphic expression of rapid Holocene
892 silicic magma reservoir growth beneath Laguna del Maule, Chile.*Science advances*,*4*(6),
893 p.eaat1513.

894 Sruoga, P., Elissondo, M., Fierstein, J., Garcia, S., Gonzalez, R., & Rosas, M. (2015). Actividad
895 explosiva postglacial del centro barrancas, complejo volcanico Laguna del Maule. In
896 *Congreso Geologico Chileno* (pp. 49–52).

897 Sruoga, P., Elissondo, M., Rosas, M., Fierstein, J., & Singer, B. S. (2018). Cerro Barrancas,
898 Laguna Del Maule Volcanic Field, Chile: unraveling its eruptive history to constrain hazard

899 assessment. In *AGU Chapman Conference*. AGU. Retrieved from
900 https://agu.confex.com/agu/18chapman1/webprogram/Paper328208.html

901 Tašárová, Z. A. (2007). Towards understanding the lithospheric structure of the southern Chilean
902 subduction zone (36°S-42°S) and its role in the gravity field. *Geophysical Journal*
903 *International*, *170*(3), 995–1014. https://doi.org/10.1111/j.1365-246X.2007.03466.x

904 Tikhonov, A. N., & Arsenin, V. Y. (1977). *Solutions of Ill-posed Problems*.

905 Till, C. B., Vazquez, J. A., & Boyce, J. W. (2015). Months between rejuvenation and volcanic
906 eruption at Yellowstone caldera, Wyoming. *Geology*, *43*(8), 695–698.
907 https://doi.org/10.1130/G36862.1

908 Till, C. B., Pritchard, M. E., Miller, C. A., Brugman, K. K., & Ryan-davis, J. (2018). Super-
909 volcanic investigations. *Nature Geoscience*. https://doi.org/10.1038/s41561-018-0100-1

910 Uieda, L. (2018). Verde: Processing and gridding spatial data using Green's functions. *Journal*
911 *of Open Source Software*, *3*(30), 957. https://doi.org/10.21105/joss.00957

912 Wespestad, C. E., Thurber, C. H., Andersen, N. L., Singer, B. S., Cardona, C., Zeng, X., et al.
913 (2019). Magma Reservoir Below Laguna del Maule Volcanic Field, Chile Imaged with
914 Surface-Wave Tomography. *Journal of Geophysical Research: Solid Earth*, 1–15.
915 https://doi.org/10.1029/2018JB016485

916 Zhan, Y., Gregg, P. M., Le Mével, H., Miller, C. A., & Cardona, C. (2019). Integrating Reservoir
917 Dynamics, Crustal Stress, and Geophysical Observations of the Laguna del Maule
918 Magmatic System by FEM Models and Data Assimilation. *Journal of Geophysical*
919 *Research: Solid Earth*, *124*(12), 13547–13562. https://doi.org/10.1029/2019JB018681

920